

# Cloud-cloud collision which triggered formation of the super star cluster RCW38

Y. Fukui<sup>1</sup>, K. Torii<sup>1</sup>, A. Ohama<sup>1</sup>, K. Hasegawa<sup>1</sup>, Y. Hattori<sup>1</sup>, S. Ohashi<sup>2,3</sup>, K. Fujii<sup>2,3</sup>, S. Kuwahara<sup>2,3</sup>, N. Mizuno<sup>3</sup>, H. Yamamoto<sup>1</sup>, K. Tachihara<sup>1</sup>, T. Okuda<sup>3</sup>, T. Onishi<sup>4</sup>, and A. Mizuno<sup>5</sup>

<sup>1</sup>Department of Physics and Astrophysics, Nagoya University, Chikusa-ku, Nagoya, Aichi 464-8601, Japan

<sup>2</sup>Department of Astronomy, School of Science, The University of Tokyo, 7-3-1 Hongo, Bunkyo-ku, Tokyo 133-0033, Japan

<sup>3</sup>National Astronomical Observatory of Japan, Mitaka, Tokyo 181-8588, Japan

<sup>4</sup>Department of Astrophysics, Graduate School of Science, Osaka Prefecture University, 1-1 Gakuen-cho, Nakaku, Sakai, Osaka 599-8531, Japan

<sup>5</sup>Solar-Terrestrial Environment Laboratory, Nagoya University, Chikusa-ku, Nagoya 464-8601, Japan

torii@a.phys.nagoya-u.ac.jp

Received \_\_\_\_\_; accepted \_\_\_\_\_

## ABSTRACT

We have found two molecular clouds having velocities of  $2\text{ km s}^{-1}$  and  $14\text{ km s}^{-1}$  toward the super star cluster RCW 38 by observations of CO ( $J=1-0$  and  $3-2$ ) transitions. The two clouds are likely physically associated with the cluster as verified by the high intensity ratio of the  $J=3-2$  emission to the  $J=1-0$  emission, the bridging feature connecting the two clouds in velocity and the morphological correspondence with the infrared dust emission. Since the total mass of the clouds and the cluster is too small to gravitationally bind the velocity, we suggest that a collision happened by chance between the two clouds. We present a scenario that the collision triggered formation of the  $\sim 20$  candidate O stars which are localized, within  $\sim 0.5\text{ pc}$  of the cluster center in the  $2\text{ km s}^{-1}$  cloud, just toward the northern tip of the  $14\text{ km s}^{-1}$  cloud. The other member low-mass stars are likely pre-existent prior to the collision since they are distributed outside the  $14\text{ km s}^{-1}$  cloud. The formation timescale of the O stars is estimated to be  $\sim 3 \times 10^4\text{ yrs}$  ( $=\sim 0.5\text{ pc}/16\text{ km s}^{-1}$ ), implying a mass accretion rate  $\sim 10^{-3} M_{\odot}\text{ yr}^{-1}$  for a  $20 M_{\odot}$  star. This is the third super star cluster alongside of Westerlund 2 and NGC 3603 where cloud-cloud collision triggered the cluster formation among the few youngest super star clusters that are associated with dusty nebulae.

*Subject headings:* ISM: clouds — radiolines: ISM

## 1. Introduction

High-mass stars are highly energetic and influential on dynamics of the interstellar medium via stellar winds, photoionization and supernova explosions at the end of their lives. Chemical enrichment of heavy elements is another important effect of high-mass stars in galactic evolution. Formation of high-mass stars is therefore one of the most important issues in astrophysics and a number of works have been published so far (for recent reviews see Zinnecker & Yorke 2007; Tan et al. 2014). It has been discussed that Core Accretion and Competitive Accretion are viable scenarios for high-mass star formation. In the Core Accretion scenario a massive dense cloud is the initial condition for the stellar cluster formation including high-mass stars, whereas in the Competitive Accretion scenario a stellar cluster/prestellar clumps of various masses are assumed to grow in mass by accretion of the ambient gas. Tan et al. (2014) discussed that star formation in these scenarios depends on the initial conditions of the cloud or the stars/clumps, and that connection with the stellar initial mass function will offer a key to test which scenario is viable as the formation mechanism of high-mass stars, whereas we do not have yet conclusive evidence for either of them.

Recent ALMA observations led to a discovery of formation of a  $37 M_{\odot}$  star triggered by collision between two filamentary clouds in N159 in the Large Magellanic Cloud (Fukui et al. 2015, hereafter Paper I). This simple system consisting of two thin filaments allows one to identify the collision which accompanies enhanced turbulent layer as is consistent with the prediction based on magneto-hydro-dynamical numerical simulations (Inoue & Fukui 2013). In the other Galactic regions of high-mass star formation we have growing evidence for triggered high-mass star formation by cloud-cloud collisions; they include two super star clusters (SSCs) NGC3603 and Westerlund 2 (Fukui et al. 2014, hereafter Paper II; Furukawa et al. 2009, Paper III; Ohama et al. 2010) and single O stars

in M 20 and RCW 120 (Torii et al. 2011, 2015). On a global scale of galaxies, numerical simulations show that collisions between clouds are fairly frequent at every 10 Myrs, which is similar to an evolutionary timescale of GMCs (Tasker & Tan 2009; Dobbs et al. 2014, 2015). It is becoming possible to consider cloud-cloud collisions as one of the dominant modes of high-mass star formation.

The characteristics of high-mass star formation by cloud-cloud collision are different from the previous scenario Core Accretion because in the cloud-cloud collision scenario dense and massive cores are not required as the initial condition. The case of N159 West indicates that a dense CS core is seen only toward the  $37 M_{\odot}$  star, and the rest of the filamentary clouds has no dense CS cores, suggesting that the initial condition is of low density, less than  $10^4 \text{ cm}^{-3}$ , even for high-mass star formation. The supersonic flow caused by the collision allows strong non-gravitational accumulation of the dense gas into a small volume very quickly within a typical timescale of  $10^5$  yrs. This becomes possible by efficient collimation of the colliding flow into a small volume of a  $1 \text{ pc}^3$  scale via the guided flow by curved magnetic field (Inoue & Fukui 2013) or by non-magnetic focusing (Takahira et al. 2014).

RCW 38 (Rodgers et al. 1960) located at 1.7 kpc from the sun is known as one of the closest high-mass star forming regions containing more than thousand stars (Wolk et al. 2006; Lada & Lada 2003) (Figure 1). At the central part of RCW 38, two remarkable infrared peaks have been identified (Frogel & Persson 1974). The brightest at  $2 \mu\text{m}$  is labeled IRS 2, which corresponds to the O5.5 binary located at the center of the RCW 38 cluster (DeRose et al. 2009). Furniss et al. (1975) derived a total infrared luminosity toward IRS 2 as  $7 \times 10^5 L_{\odot}$ . On the other hand, the brightest in  $10 \mu\text{m}$  is found 0.1 pc west of IRS 2, and is labelled IRS 1. IRS 1 is a dust ridge extending by 0.1–0.2 pc in the north-south direction (Figure 1b), which has a color temperature of about 175 K and includes several

condensations (Smith et al. 1999).

Infrared and millimeter radio observations has indicated a “ring-like” or “horseshoe” structure around IRS 2 about  $1' - 2'$  across (Figure 1; Huchtmeier 1974; Vigil 2004; Wolk et al. 2006, 2008). Inside the ring-like shape two regions are cleared of dust and forms cavities, one is the region centered on IRS 2 with a diameter of  $\sim 0.1$  pc, and another is just west of IRS 1 with a similar size (Smith et al. 1999; Wolk et al. 2008), suggesting that they were formed by feedbacks from high-mass stars. A large-area infrared image shows that RCW 38 includes numerous filaments and bubbles (see Figure 1a). Kaneda et al. (2013) discussed, using the AKARI infrared satellite observations, that the extended infrared emission is attributed to the polycyclic aromatic hydrocarbon (PAH), warm dust grains detectable at mid-infrared, and cool dust grains at far-infrared along the line-of-sight. They also observed [CII]  $158\mu\text{m}$  line which suggests that PAHs play a relatively important role for photo-electric heating of gas in photo-dissociation regions (PDRs) in the central  $\sim 3$  pc of RCW 38.

Condition of the HII region has been investigated by radio continuum and recombination line observations; an electron temperature of  $\sim 8000$  K, an emission measure of  $\sim 10^6 \text{ pc cm}^{-6}$ , and  $v_{\text{LSR}}$  and  $\Delta v$  of the recombination line is  $+1 \text{ km s}^{-1}$  and over  $30 \text{ km s}^{-1}$ , respectively (Huchtmeier 1974; McGee & Newton 1981; Caswell & Haynes 1987). A relatively high electron density of  $\sim 10^4 \text{ cm}^{-3}$  suggests that the HII region is confined by the surrounding material and forms a compact HII region. On the other hand, stellar winds, hot plasma, HII gas, and UV photons are partly escaping from the confinement, as shown by the extended infrared emission, diffuse X-ray emission, and radio continuum emission (Wolk et al. 2002; Vigil 2004), providing a significant effect on the ambient medium (Wolk et al. 2008).

Many observational studies to investigate the cluster members of RCW 38 have been

carried out so far. Near infrared observations by using the Very Large Telescope (VLT) identified more than 300 young stars for the  $\sim 0.5 \text{ pc}^2$  area centered on IRS 2 (DeRose et al. 2009). *Chandra* observations reported by Wolk et al. (2006) was used to identify 345 X-ray sources likely associated with RCW 38. Completeness arguments suggest a total estimated cluster size of between 1500 and 2400 stars. Winston et al. (2011) identified 624 young stellar objects (YSOs) the *Spitzer*/IRAC observations toward a  $30' \times 30'$  region of RCW 38. In addition, about sixty O-star candidates have been identified by Wolk et al. (2006) and Winston et al. (2011) in a large area of RCW 38, and estimated the age of the RCW 38 cluster to be 0.5 Myrs. Out of them, about twenty O-star candidates are found in the central  $\sim 1 \text{ pc}$  (Wolk et al. 2006).

Molecular line observations toward RCW 38 are very limited. Yamaguchi et al. (1999) observed a large area of RCW 38 and found that a molecular cloud which coincides with IRS 2, although detailed structures including the ring-like component were not resolved due to a relatively coarse resolution. On the other hand, Zinchenko et al. (1995) observed the central region of RCW 38 at HPBW of  $\sim 1'$  in the CS emission to resolve the ring shape surrounding IRS 2.  $^{12}\text{CO } J=1-0$  observations with SEST at  $45''$  resolution for a small  $160'' \times 160''$  region performed by Gyulbudaghian & May (2008) show two molecular clouds likely associated with RCW 38 at two different velocity ranges of  $-3 - +2 \text{ km s}^{-1}$  and  $+3 - +8 \text{ km s}^{-1}$ .

An overview of the previous studies on RCW 38 is summarized in an article in the Handbook of Star Formation (Wolk et al. 2008).

In this paper, we present new molecular line observations toward RCW 38 obtained with NANTEN2, Mopra, and ASTE telescopes. The NANTEN2 CO  $J=1-0$  observations covered a large area of RCW 38 at a angular resolution of  $4'$  to describe the large scale molecular morphologies and velocities, while the Mopra CO  $J=1-0$  and ASTE CO

$J=3-2$  observations at angular resolutions of  $22''-35''$  revealed the detailed molecular gas distributions and physical conditions such as temperature and density around IRS 1 and IRS 2.

## 2. Observations

### 2.1. NANTEN2 CO $J=1-0$ observations

The NANTEN2 4-m mm/sub-mm telescope situated in Chile was used to observe a large area  $1.8^\circ \times 1.8^\circ$  of RCW 38 in the  $^{12}\text{CO}$  and  $^{13}\text{CO}$   $J=1-0$  transitions during from May 2012 to December 2012. The 4 K cooled SIS mixer receiver equipped with NANTEN2 provided a typical system temperature  $T_{\text{sys}}$  of  $\sim 250$  K in DSB. The backend was a digital spectrometer which provides 16384 channels at 1 GHz bandwidth and 61 kHz resolution, which corresponds to  $2600 \text{ km s}^{-1}$  and  $0.17 \text{ km s}^{-1}$ , respectively, at 110 GHz. The obtained data was smoothed to a velocity resolution of  $0.8 \text{ km s}^{-1}$  and angular resolution of  $240''$ . The pointing accuracy was checked to be less than  $15''$  with daily observations toward the Sun and IRC 10216 (R.A., Dec.)=( $9^{\text{h}} 47^{\text{m}} 57^{\text{s}}.406$ ,  $13^\circ 16' 43''.56$ ). The absolute intensity calibration was done with daily observations of the  $\rho$ -Ophiuchus molecular cloud (Ra., Dec.)=( $16^{\text{h}} 32^{\text{m}} 23^{\text{s}}.3$ ,  $-24^\circ 28' 39''.2$ ) and Perseus molecular cloud (Ra., Dec.)=( $3^{\text{h}} 29^{\text{m}} 19^{\text{s}}.0$ ,  $31^\circ 24' 49''.0$ ).

### 2.2. Mopra CO $J=1-0$ observations

Detailed CO  $J=1-0$  distributions around RCW 38 were obtained by using the 22-m ATNF (Australia Telescope National Facility) Mopra mm telescope in Australia at a high spatial resolution of  $33''$  during July 2012. We simultaneously observed  $^{12}\text{CO}$   $J=1-0$ ,  $^{13}\text{CO}$   $J=1-0$ , and  $\text{C}^{18}\text{O}$   $J=1-0$  toward a  $11' \times 15'$  area of RCW 38 with the OTF mode with a

unit field of  $4' \times 4'$ .  $T_{\text{sys}}$  was 400–600 K in the SSB. The Mopra backend system “MOPS” which provides 4096 channels across 137.5 MHz in each of the two orthogonal polarizations was used in the observations. The velocity resolution was  $0.088 \text{ km s}^{-1}$  and the velocity coverage was  $360 \text{ km s}^{-1}$  at 115 GHz. The obtained data was smoothed to be HPBW of  $40''$  with a 2D Gaussian function and to a  $0.6 \text{ km s}^{-1}$  velocity resolution. The pointing accuracy was checked every 1 hour to keep within  $7''$  with observations of 86 GHz SiO masers. We made daily observations of Orion-KL (R.A., Dec.)= $(-5^{\text{h}}35^{\text{m}}14^{\text{s}}.5, -5^{\circ}22'29''.6)$  to estimate “extended beam efficiency” by making comparisons with the peak temperature of 100 K in Orion-KL shown in Figure 6 of Ladd et al. (2005). We finally obtained an extend beam efficiency of 0.48.

### 2.3. ASTE $^{12}\text{CO } J=3-2$ observations

CO  $J=3-2$  line observations of RCW 38 were performed by using the ASTE 10-m telescope located in Chile in 2013. The waveguide-type sideband-separating SIS mixer receiver for the single sideband (SSB) “CAT345” and the digital spectrometer “MAC” with the narrow-band mode providing 128 MHz bandwidth and 0.125 MHz resolution, which corresponds to  $111 \text{ km s}^{-1}$  velocity coverage and  $0.11 \text{ km s}^{-1}$  velocity resolution at 345 GHz, was used. The observations were made with the OTF mode at a grid spacing of  $7.5''$ , and the HPBW was  $22''$  at the CO  $J=3-2$  frequency.

## 3. Results

### 3.1. Large scale molecular distributions with NANTEN2

We first present large scale molecular distributions of RCW 38 using the NANTEN2  $^{12}\text{CO } J=1-0$  dataset. Compared with the NANTEN observations given by Yamaguchi et al.



(1999), although the beam size of  $180''$  is the same, the grid spacing of  $60''$  in the present NANTEN2 observations is quarter, which enables us to reveal the gas distributions into more detail.

As shown in the CO distributions in Figure 2, toward the direction of RCW 38, two CO clouds are distributed at radial velocities  $v_{\text{LSR}}$  of  $-4 - +8 \text{ km s}^{-1}$  and  $+9 - +14 \text{ km s}^{-1}$ . In Figure 2(a), the blue-shifted cloud has a remarkably strong peak just coinciding with the center part of RCW 38. The compact peak with a size of  $0.1$  ( $\sim 3 \text{ pc}$  at RCW 38) has a trailing feature elongated toward the southwest of RCW 38, showing a characteristic “head-tail” structure, which was also detected in Yamaguchi et al. (1999). The head-tail structure is surrounded by the diffuse CO emission distributed around  $v_{\text{LSR}}$  of  $0 - +8 \text{ km s}^{-1}$ , covering the present observed region.

Contrary to the blue-shifted cloud, as shown in Figure 2(b), the red-shifted cloud has weak and dispersed CO distribution. A CO peak at  $(l, b \sim 268^\circ 0, -1^\circ 1)$  with relatively strong emission is located at just the southeast of RCW 38, pointing toward the center of RCW 38. This CO peak is well covered with the Mopra and ASTE observations as indicated by a box with solid lines in Figure 2(b). There are several other CO components around the CO peak, and they all seem to be continuously distributed along the east-west direction roughly at a range of  $(l, b) \sim (267^\circ 5, -1^\circ 2) - (268^\circ 4, -0^\circ 9)$ . In the position-velocity diagram in Figure 2(c), the red-shifted cloud can be identified separately from, although it looks being connected with, the blue-shifted cloud and the diffuse emission, suggesting a possible physical relationship of the red-shifted cloud with RCW 38.

### 3.2. Detailed molecular distributions with Mopra and ASTE

We present the detailed molecular distributions around the center region of RCW 38 using the Mopra and ASTE datasets. In Figure 3, the integrated intensity maps (left and center panels) and the position-velocity maps (right panels) are shown with  $^{12}\text{CO}$   $J=3-2$  (upper panels) and  $^{13}\text{CO}$   $J=1-0$  (lower panels). In Figure 3(a) and (d), the outstanding compact peak seen in Figure 2(a) is resolved. It shows a ring-like structure having a diameter of 1–1.5 pc, forming a cavity centered on IRS 2, and several filamentary and bubble-like structures are radially extended outside the ring-like structure by 1–2 pc. In the  $^{12}\text{CO}$  position-velocity diagram in Figure 3(c), intensity decrease is seen around  $v_{\text{LSR}}$  of 0–2 km s $^{-1}$ . The  $^{13}\text{CO}$  in Figure 3(f) shows a single peak at  $\sim 2$  km s $^{-1}$ , indicating that the dip at the same velocity in the  $^{12}\text{CO}$  is due to self-absorption. We hereafter call the blue-shifted cloud and the red-shifted cloud the 2 km s $^{-1}$  cloud and the 14 km s $^{-1}$  cloud, respectively.

The ring-like structure in  $^{13}\text{CO}$  consists of four clumps (clumps A–D), and the ring-like structure itself has an elongated shape along the northeast-southwest direction. The sizes of the clumps range from 0.3 pc to 0.5 pc, and  $\Delta v$  from  $\sim 4$  km s $^{-1}$  to 5 km s $^{-1}$ .

In contrast to the complicated distributions of the 2 km s $^{-1}$  cloud, the 14 km s $^{-1}$  cloud has a simple ridge elongated from the north to the south (Figures 3b and 3e). Since  $^{12}\text{CO}$  and  $^{13}\text{CO}$  show similar distributions in the position-velocity map in Figures 3(c) and (f), the 14 km s $^{-1}$  cloud is likely less affected by self-absorption in  $^{12}\text{CO}$ .

At its bottom, the ridge intersects another elongated structure running from the east to the west, and these two orthogonal elongated structures comprise the 14 km s $^{-1}$  cloud in the present observing area. As shown in Figures 3(c) and 3(f), the 14 km s $^{-1}$  cloud shows a uniform velocity gradient of 1 km s $^{-1}$  pc $^{-1}$  along the ridge. We find a connecting feature in velocity between the CO emission of the 2 km s $^{-1}$  cloud and the 14 km s $^{-1}$  cloud at

$\sim 6 \text{ km s}^{-1}$  and  $\sim 14 \text{ km s}^{-1}$ , respectively, and it is not seen beyond the velocity of the blue cloud. The weak emission around the declination of  $-47^\circ 27'5$ , whose R.A. is  $8^{\text{h}}59^{\text{m}}15^{\text{s}}$ , seems to be located on an extension of this velocity gradient, suggesting that it is possibly part of the  $14 \text{ km s}^{-1}$  cloud.

### 3.3. Intensity ratios of $^{12}\text{CO } J=3-2$ to $^{12}\text{CO } J=1-0$

In order to investigate the physical properties of the  $14 \text{ km s}^{-1}$  cloud and the  $2 \text{ km s}^{-1}$  cloud, we present distributions of the intensity ratio of  $^{12}\text{CO } J=3-2$  to  $^{12}\text{CO } J=1-0$  (hereafter  $R_{3-2/1-0}$ ). Taking intensity ratios between different  $J$ -level CO is a useful diagnose of the molecular gas properties (e.g., Ohama et al. 2010; Torii et al. 2011; Fukui et al. 2014).

As seen in the  $R_{3-2/1-0}$  position-velocity diagram in Figure 7, both of the  $2 \text{ km s}^{-1}$  cloud and the  $14 \text{ km s}^{-1}$  cloud have typical ratios of  $0.6-0.8$ , up to over  $1.0$ . Since the  $2 \text{ km s}^{-1}$  cloud is strongly affected by the self-absorption in  $^{12}\text{CO}$  spectra around its central velocity range,  $\sim 0-4 \text{ km s}^{-1}$ , the ratios around this velocity range is not reliable. On the other hand, low intensity ratios are seen at the northern part (declination  $> -47^\circ 27'$ ) and southern part (declination  $< -47^\circ 34'$ ) of the  $2 \text{ km s}^{-1}$  cloud, where the diffuse CO emission is widely distributed, while the  $14 \text{ km s}^{-1}$  cloud retains its relatively high intensity ratios of  $\sim 0.6-0.8$  throughout the cloud.

### 3.4. Temperature and density of the molecular gas

We here utilize the large velocity gradient (LVG) analysis (e.g., Goldreich & Kwan 1974) to estimate kinetic temperature  $T_{\text{k}}$  and molecular number density  $n(\text{H}_2)$  of the  $14 \text{ km s}^{-1}$  cloud and the  $2 \text{ km s}^{-1}$  cloud to interpret their intensity ratio distributions.

We first present curves of  $R_{3-2/1-0}$  as a function of  $T_k$  in Figure 8 for various densities from  $10^2 \text{ cm}^{-3}$  to  $10^4 \text{ cm}^{-3}$ , where two  $X(\text{CO})/(dv/dr)$  of  $10^{-5} (\text{km s}^{-1} \text{ pc}^{-1})^{-1}$  and  $3 \times 10^{-6} (\text{km s}^{-1} \text{ pc}^{-1})^{-1}$  are assumed. We here adopt an abundance ratio  $X(\text{CO}) = [^{12}\text{CO}]/[\text{H}_2] = 10^{-4}$  (e.g., Frerking et al. 1982; Leung et al. 1984), and typical  $dv/dr$  is estimated for clumps A–D as  $4 \text{ km s}^{-1}/0.4 \text{ pc} = 10 \text{ km s}^{-1} \text{ pc}^{-1}$  and  $10 \text{ km s}^{-1}/0.3 \text{ pc} \sim 33 \text{ km s}^{-1} \text{ pc}^{-1}$ , respectively.

Figure 8 provides a useful guide for the  $R_{3-2/1-0}$  distributions in Figures 7. If  $R_{3-2/1-0}$  is larger than 0.7, which is depicted by a dashed line in Figure 8,  $T_k$  is always higher than 10 K for every  $n(\text{H}_2)$ . 10 K is a typical value of the galactic molecular gas without any star formation, suggesting that the gas with  $T_k$  higher than 10 K is heated by some additional heating. On the other hand, if  $R_{3-2/1-0}$  is as small as 0.4,  $T_k$  cannot be determined, since it has a large variation from  $<10 \text{ K}$  to  $>100 \text{ K}$  depending on  $n(\text{H}_2)$ .

Both of the  $2 \text{ km s}^{-1}$  cloud and the  $14 \text{ km s}^{-1}$  cloud show  $R_{3-2/1-0}$  of higher than 0.7 and up to over 1.0 at many points, suggesting that these two clouds have  $T_k$  higher than 10 K. It is reasonable that the heating is due to the O stars in RCW38. On the other hand, the physical condition of the diffuse CO emission surrounding the  $2 \text{ km s}^{-1}$  cloud with  $R_{3-2/1-0}$  of 0.4 is unclear.

In order to provide more quantitative constraints for  $T_k$  and  $n(\text{H}_2)$ , we here add the ratio of  $^{13}\text{CO } J=1-0$  to  $^{12}\text{CO } J=1-0$  (hereafter  $R_{13/12}$ ) in the LVG analysis, with an assumption of the abundance ratio  $[^{12}\text{CO}]/[^{13}\text{CO}] = 77$  (Wilson & Rood 1994). Ten target regions are finally chosen (regions A–J) in the  $2 \text{ km s}^{-1}$  cloud and the  $14 \text{ km s}^{-1}$  cloud for  $T_k$  and  $n(\text{H}_2)$  estimates. The CO spectra and the LVG results are presented in Figures 9 and 10 for the individual target regions. In the CO spectra, the velocity ranges used for the LVG analysis are shown by shade. For the  $2 \text{ km s}^{-1}$  cloud, the five target regions are chosen not to have apparent self-absorption in their  $^{12}\text{CO}$  spectra. For the  $2 \text{ km s}^{-1}$  cloud, regions

A–C are taken around the rim of the dense part, while regions D and E are at the low  $R_{3-2/1-0}$  regions widely distributed in the north and the south. On the other hand, regions F–J in Figure 10 are taken to cover a large area of the  $14\text{ km s}^{-1}$  cloud. In the diagrams of the LVG results,  $R_{3-2/1-0}$  and  $R_{13/12}$  distributions are shown with the blue lines and red lines, respectively, and their errors are shown with the colored area. Here the errors are estimated with  $1\sigma$  fluctuations of the spectra and 10% relative calibration error for each CO transition. Since  $^{12}\text{CO } J=1-0$  and  $^{13}\text{CO } J=1-0$  were taken simultaneously with the same receiver and the same backend at Mopra, we here assume that the 10% relative calibration error is canceled for  $R_{13/12}$ , and is adopted only for  $R_{3-2/1-0}$ . In addition,  $dv/dr$  is estimated for individual regions, and  $X(\text{CO})$  is assumed to be  $10^{-4}$  same as in Figure 8. Finally,  $T_k$  and  $n(\text{H}_2)$  are given at the region where  $R_{3-2/1-0}$  curve and  $R_{13/12}$  curve overlap.

The results are summarized as follows: Regions A–C in the  $2\text{ km s}^{-1}$  cloud and all regions in the  $14\text{ km s}^{-1}$  cloud (regions F–J) show  $T_k$  of higher than 10 K, typically 30–40 K and up to more than 50 K. Typical  $n(\text{H}_2)$  for these regions are about  $10^3\text{--}10^4\text{ cm}^{-3}$ , where only lower limits are given for regions A, B, and F2 and no solutions are given for regions F1 and I. On the other hand, regions D and E located at the south of the  $2\text{ km s}^{-1}$  cloud show significantly low  $T_k$  less than 10 K and  $n(\text{H}_2)$  of  $\sim 3 \times 10^3\text{ cm}^{-3}$ .

As a summary, both of the  $2\text{ km s}^{-1}$  cloud and the  $14\text{ km s}^{-1}$  cloud show remarkably high temperatures of  $T_k > 20\text{--}30\text{ K}$ . Some heating source/mechanism is necessary to understand the results, and radiative heating by the O stars in RCW 38 is a reasonable candidate. It is emphasized that the present results suggest that, despite of a large velocity separation of  $\sim 10\text{ km s}^{-1}$ , both of the  $2\text{ km s}^{-1}$  cloud and the  $14\text{ km s}^{-1}$  cloud are associated with RCW 38.

### 3.5. Molecular masses of the $2 \text{ km s}^{-1}$ cloud and the $14 \text{ km s}^{-1}$ cloud

By adopting the distance of RCW 38,  $1.7 \text{ kpc}$ , to both the  $2 \text{ km s}^{-1}$  cloud and the  $14 \text{ km s}^{-1}$  cloud, their molecular masses can be estimated. We first estimate the molecular mass by using the  $X(\text{CO})$  factor, which is an empirical conversion factor from  $^{12}\text{CO } J=1-0$  integrated intensity into  $\text{H}_2$  column density. We hereafter refer to the molecular mass estimated with a  $X(\text{CO})$  factor as  $M_{X(\text{CO})}$ . As already stated, since  $^{12}\text{CO}$  is strongly affected by the self-absorption in particular in the central  $1-2 \text{ pc}$  of RCW 38,  $M_{X(\text{CO})}$  may be underestimated. It is, however, still quite useful to estimate  $M_{X(\text{CO})}$  to give the lower limit of the molecular mass. We here assume an  $X(\text{CO})$ -factor of  $2 \times 10^{20} \text{ cm}^{-2} (\text{K km s}^{-1})^{-1}$  (Strong et al. 1988).

Using the NANTEN CO dataset,  $M_{X(\text{CO})}$  in the central peak of the  $2 \text{ km s}^{-1}$  cloud seen in Figure 2(a) is estimated to be  $3.0 \times 10^3 M_\odot$ , for the points with the  $^{12}\text{CO } J=1-0$  integrated intensity  $W(^{12}\text{CO}1-0)$  equal or larger than  $65 \text{ K km s}^{-1}$ , and  $M_{X(\text{CO})}$  of the head-tail structure depicted by dashed line in Figure 2(a) is  $1.7 \times 10^4 M_\odot$  at  $W(^{12}\text{CO}1-0) \geq 30 \text{ K km s}^{-1}$ . On the other hand,  $M_{X(\text{CO})}$  of the  $14 \text{ km s}^{-1}$  cloud at the region depicted by dashed lines in Figure 2(b) is  $2.6 \times 10^3 M_\odot$ , one order of magnitude smaller than that of the  $2 \text{ km s}^{-1}$  cloud.

$M_{X(\text{CO})}$  of the central peak of the  $2 \text{ km s}^{-1}$  cloud is also estimated using the Mopra  $^{12}\text{CO } J=1-0$  dataset (Figure 3) to be  $4.6 \times 10^3 M_\odot$  at  $W(^{12}\text{CO}1-0) \geq 70 \text{ K km s}^{-1}$ , and that in the ring structure in the inner  $1-1.5 \text{ pc}$  is  $1.9 \times 10^3 M_\odot$  ( $W(^{12}\text{CO}1-0) \geq 140 \text{ K km s}^{-1}$ ). On the other hand,  $M_{X(\text{CO})}$  of the  $2 \text{ km s}^{-1}$  cloud in Figure 3(b) is calculated to be  $1.2 \times 10^3 M_\odot$  at  $W(^{12}\text{CO}1-0) \geq 10 \text{ K km s}^{-1}$ .

We next estimate the molecular mass of the central ring-like structure in the  $2 \text{ km s}^{-1}$  cloud using the Mopra  $^{13}\text{CO } J=1-0$  data with the local thermodynamic equilibrium (LTE) assumption. In estimate of the molecular mass with a LTE assumption (hereafter  $M_{\text{LTE}}$ ),

excitation temperature  $T_{\text{ex}}$  must be provided, and the peak intensity of the  $^{12}\text{CO } J=1-0$  emission  $T(^{12}\text{CO})$  is usually used to estimate  $T_{\text{ex}}$  with the following equation (ref),

$$T_{\text{ex}} = \frac{5.53}{\ln\{1 + 5.53/(T(^{12}\text{CO}) + 0.819)\}}. \quad (1)$$

Although the  $^{12}\text{CO } J=1-0$  emission strongly suffers from the self-absorption as shown in the spectra for clumps A–D, their observed brightness temperature is still remarkably as high as up to 45 K in clump C, which corresponds to  $T_{\text{ex}}$  of 49 K with equation 1. This figure is roughly consistent with the LVG analysis resulting in  $T_{\text{k}} > 30-50$  K (Figure 9) in regions A–C which are located in the outskirts of the  $2 \text{ km s}^{-1}$  cloud. We therefore adopt an uniform  $T_{\text{ex}}$  of 49 K in the present  $M_{\text{LTE}}$  estimates.

$M_{\text{LTE}}$  of the ring-like structure shown in Figure 3d is finally estimated to be  $5.2 \times 10^3 M_{\odot}$  at the  $^{13}\text{CO } J=1-0$  integrated intensity  $W(^{13}\text{CO}1-0) \geq 22.5 \text{ K km s}^{-1}$ , which is by a factor of 2.7 larger than  $M_{X(\text{CO})}$  in the ring-like structure. The present estimate also provides a remarkably high  $\text{H}_2$  column density  $N(\text{H}_2)$  of  $1 \times 10^{23} \text{ cm}^{-2}$  as a typical value in the ring-like structure. On the other hand,  $M_{\text{LTE}}$  and typical  $N(\text{H}_2)$  of the central cavity surrounded by the ring-like structure is estimated to be  $120 M_{\odot}$  and  $3 \times 10^{22} \text{ cm}^{-2}$ , suggesting that the ring-like structure is actually a two-dimensional structure, not a three dimensional shell.  $M_{\text{LTE}}$  of the four  $^{13}\text{CO}$  clumps shown in Figure 6a are estimated at  $W(^{13}\text{CO}1-0) \geq 32.5 \text{ K km s}^{-1}$ , and the results are given as follows:  $1.0 \times 10^3 M_{\odot}$  for clump A,  $8.8 \times 10^2 M_{\odot}$  for clump B,  $5.7 \times 10^2 M_{\odot}$  for clump C, and  $5.6 \times 10^2 M_{\odot}$  for clump D. These results are also summarized in Table 1.

### 3.6. Comparisons with infrared images

Figure 12 shows velocity channel distributions of CO overlayed on the infrared image, which consists of several filamentary features around the central peak toward the cluster

(Kaneda et al. 2013). We present the major infrared features, labeled by a–h, as indicated by the dashed lines in the first panel of Figure 12. The  $2\text{ km s}^{-1}$  cloud is ring-shaped, clearly indicating the ionizing dispersal due to the cluster, and is associated with all the infrared features at around  $-4-+3\text{ km s}^{-1}$ . The association of the  $2\text{ km s}^{-1}$  cloud is verified by the correspondence. The  $14\text{ km s}^{-1}$  cloud is associated with the two infrared features f and g as suggested by the correspondence. We further note that the  $14\text{ km s}^{-1}$  cloud is probably responsible for IRS 2 which is distributed in the north-south direction and is clearly irradiated by the cluster, whereas the current resolution is not high enough to test details of the CO distribution with the infrared image. By considering the enhanced line intensity ratio in Section 3.3, which indicates the high temperature due to radiative heating, we see unambiguous evidence for the association of the two clouds with the cluster.

YSOs and O star candidates plotted in Figure 11(b) are concentrated toward the central few pc of RCW 38. In particular, many class I YSOs depicted by red circles are seen inside the four dense clumps, suggesting star formation within the clumps. YSOs are also seen inside the trailing feature. O star candidates are strongly concentrated toward the central cavity surrounded by the ring structure, suggesting that the cavity was formed by the feedbacks of these O-star candidates.

## 4. Discussion

### 4.1. The two clouds; physical association and evidence for collision

The present observations have revealed two molecular clouds with  $12\text{ km s}^{-1}$  velocity separation toward the super star cluster RCW 38. The following pieces of evidence offer robust verification of the association between the two clouds and the cluster.

1. The  $2\text{ km s}^{-1}$  cloud shows a hole toward the cluster and is ring shaped. The cloud is



also associated with the infrared filamentary features heated by the cluster. These morphological correspondences show the physical association of the cloud with the cluster. The  $14 \text{ km s}^{-1}$  cloud also shows a good correspondence with the depression of the infrared emission elongated in the south (see  $12.7\text{--}15.1 \text{ km s}^{-1}$  panel in Figure 12).

2. The line intensity ratio of the  $^{12}\text{CO } J=3\text{--}2$  emission to  $^{13}\text{CO } J=1\text{--}0$  emission shows significantly high values, corresponding to high gas temperatures toward the cluster. LVG calculations show that the temperature there is as high as 30 K, consistent with local heating by the O stars in the cluster. It is also possible that shock heating may provide additional heating which also support the physical interaction between the two clouds with the cluster.
3. An additional sign of the interaction between the clouds is seen as the bridging features between the clouds in velocity at least in three places including the direction of the cluster center as described in section 3.

The cloud velocity separation is large  $12 \text{ km s}^{-1}$  as seen in the previous two cases Westerlund 2 and NGC 3603 studied in Papers I and II. The velocity is too large to be gravitationally bound by the total mass of the clouds and cluster,  $10^5 M_{\odot}$ . This indicates that the cloud encounter is by chance, while the relatively rich molecular density in the Vela ridge region (Yamaguchi et al. 1999, 2001) may favor more frequent collisions than elsewhere in the Galaxy, for instance in the inter-arm regions.

#### 4.2. RCW38 as the youngest SSC in the Galaxy

The number of super star clusters in the Galaxy is small, only 20 at most, as listed in the review (Portegies Zwart et al. 2010). All these clusters harbor  $\sim 30$  O stars and the ionization of the surrounding medium is strong. According to eye inspection of the

infrared and molecular images, only four clusters, NGC 3603, RCW 38, Westerlund 2 and DSB[2003]179, are associated with dusty nebulousity. Rests of the clusters have no associated nebulousity; the most typical cases are seen in the Arches and Quintuplet clusters where the nebulousity is completely dispersed by the stellar feedback.

RCW 38 is different from the previous two cases of cloud-cloud collision, NGC 3603 and Westerlund 2, in that the nebulous dusty material is still rich even toward the cluster (see Spitzer image in Figure 1, Kaneda et al. 2013). This suggests that RCW 38 is the youngest cluster studied so far in the context of super star cluster formation, and is consistent with that there is plenty of molecular gas within projected radius of 0.3 pc of the cluster. This is a unique feature of RCW 38 not seen in the other two and provides an opportunity to study the initial conditions of the super star cluster formation. Figure 13 shows the averaged CO intensity in the three cluster RCW38, NGC3603, and Westerlund2, indicating that RCW38 has the largest molecular mass within a few pc of the cluster. In the other two cases Westerlund 2 and NGC 3603 the central parts of the clouds are already strongly ionized; ionized radii are a few pc for Westerlund 2 and 0.5 pc for NGC 3603 corresponding to a typical age of  $\sim 2$  Myrs.

The only partial ionizing dispersal of the molecular gas in RCW 38 allows us to study the collisional process in the stage of cluster formation earlier than NGC 3603 and Westerlund 2. In this context, it is of particular interest to look into the initial conditions prior to the collision. In Figure xx we find the distribution of the  $14 \text{ km s}^{-1}$  cloud and the bridging feature show a good spatial correlation with the O star candidates. This offers a support for that the cloud-cloud collision preferentially triggered O star formation but not the low-mass stars. Star formation occurred extensively for lower-mass stars in the  $2 \text{ km s}^{-1}$  cloud prior to the cloud-cloud collision. This is supported by the spatially extended distribution of the YSOs outside the inner ring of the  $2 \text{ km s}^{-1}$  cloud in Figure 11.

A similar duality in stellar age is found in NGC 3603 (?), supporting a clear indication of at least two epochs of star formation. The youngest one is in the central 0.2 pc where O stars are exceptionally rich. By assuming that the relative cloud motion is inclined to the line of sight by 45 degrees, we estimate the actual relative velocity of the two clouds is  $17 \text{ km s}^{-1}$ . The radius of the cluster’s influence is seen to be about 0.3 pc in radius as indicated by the hole in the molecular distribution (Figure 11). We estimate the typical collision timescale to be very short,  $0.3 \text{ pc} / 17 \text{ km s}^{-1} = 0.2 \text{ Myrs}$ .

The stellar spectral types are not well constrained yet in part due to the heavy obscuration in RCW38. The ionization nonetheless offers a robust limit for the typical mass of the O stars to be more than  $20 M_{\odot}$  for the total UV photons estimated by radio continuum observations. Concerning the timescale of high-mass star formation, it has been shown that the youngest stars are formed coevally in the order of  $10^5 \text{ yrs}$  in NGC3603 and Westerlund 2 by careful measurements of stellar ages with HST and VLT (Kudryavtseva et al. 2012). Since the highest-mass stars have 30–100  $M_{\odot}$  in these clusters, the mass accretion rate is estimated to be  $3 \times 10^{-4} M_{\odot} \text{ yr}^{-1}$  to  $10^{-3} M_{\odot} \text{ yr}^{-1}$  as is consistent with the present case.

## 5. Conclusions

We have carried out CO  $J=1-0$  and  $J=3-2$  observations toward the super star cluster RCW 38 with NANTEN2, ASTE and Mopra mm/sub-mm telescopes. The main conclusions of the present study are summarized as follows;

1. We have observed two molecular clouds at velocities of  $2 \text{ km s}^{-1}$  and  $14 \text{ km s}^{-1}$  toward RCW 38. The  $2 \text{ km s}^{-1}$  cloud shows a ring-like shape with a cavity inside the ring ionized by the cluster and has a high molecular column density of  $\sim 10^{23} \text{ cm}^{-2}$ . The

other has a finger-like shape whose tip is toward the cluster and has a low molecular column density of  $10^{21} \text{ cm}^{-2}$ . The total masses of the  $2 \text{ km s}^{-1}$  cloud and the  $14 \text{ km s}^{-1}$  cloud are  $1.7 \times 10^4 M_{\odot}$  and  $2.6 \times 10^3 M_{\odot}$ , respectively.

2. It is likely that the two clouds are physically associated with the cluster as verified by the high ratio of the  $J=3-2$  transition to the  $J=1-0$  transition,  $R_{3-2/1-0}$ , toward the cluster. The observed ratio indicates kinetic temperature of 30 K according to the LVG calculations, which is significantly higher than the usual molecular cloud temperature 10 K with no extra heat source. The association is further supported by the similar distribution of the molecular clouds with the infrared dust features heated by the cluster; the  $2 \text{ km s}^{-1}$  cloud shows remarkable correlation with the extend dust features, and the  $14 \text{ km s}^{-1}$  cloud possibly corresponds the infrared ridge called IRS 2 toward the cluster. In addition, the two clouds are linked with each other by bridging features in velocity at least in three places including the direction of the cluster, suggesting the physical connection between the two clouds.
3. Since the total mass of the clouds and the cluster is too small to gravitationally bind the velocity, we suggest that the clouds encountered by chance. We present an interpretation that the two clouds collided with each other to form the high-mass stars in the cluster 0.4 Myrs ago at  $16 \text{ km s}^{-1}$  for an assumed cloud relative motion of 45 degrees to the line of sight. The collision took place  $0.3 \text{ pc} / 17 \text{ km s}^{-1} = 0.2 \text{ Myr}$  ago and the 20 O star candidates were formed in this timescale with the mass accretion rate  $10^{-4} M_{\odot} \text{ yr}^{-1}$  for an assumed stellar mass  $20 M_{\odot}$  and the collision timescale. The column density of the  $2 \text{ km s}^{-1}$  cloud,  $\sim 10^{23} \text{ cm}^{-2}$ , is ten-times higher than that of the  $14 \text{ km s}^{-1}$  cloud.
4. RCW 38 is the third super star cluster alongside Westerlund 2 and NGC 3603 where cloud-cloud collisions triggered the cluster formation, lending further support for a

crucial role of collision in high-mass star formation. Among the three RCW 38 is unique because it is the youngest cluster where the initial conditions prior to the star formation may still hold without cloud dispersal by ionization. The tip of the  $14 \text{ km s}^{-1}$  cloud and the bridging features connecting the two clouds well coincides with the youngest high-mass stars within  $0.3 \text{ pc}$  of the cluster center, indicating that the triggering happened only toward the inner  $0.3 \text{ pc}$  and the other member stars outside  $0.3 \text{ pc}$  are pre-existent prior to the collision.

## REFERENCES

- Caswell, J. L., & Haynes, R. F. 1987, *A&A*, 171, 261
- DeRose, K. L., Bourke, T. L., Gutermuth, R. A., et al. 2009, *AJ*, 138, 33
- Dobbs, C. L., Pringle, J. E., & Duarte-Cabral, A. 2015, *MNRAS*, 446, 3608
- Dobbs, C. L., Pringle, J. E., & Naylor, T. 2014, *MNRAS*, 437, L31
- Frerking, M. A., Langer, W. D., & Wilson, R. W. 1982, *ApJ*, 262, 590
- Frogel, J. A., & Persson, S. E. 1974, *ApJ*, 192, 351
- Fukui, Y., Ohama, A., Hanaoka, N., et al. 2014, *ApJ*, 780, 36
- Fukui, Y., Harada, R., Tokuda, K., et al. 2015, *ArXiv e-prints*, arXiv:1503.03540, submitted to *ApJL*
- Furniss, I., Jennings, R. E., & Moorwood, A. F. M. 1975, *ApJ*, 202, 400
- Furukawa, N., Dawson, J. R., Ohama, A., et al. 2009, *ApJ*, 696, L115
- Goldreich, P., & Kwan, J. 1974, *ApJ*, 189, 441
- Gyulbudaghian, A. L., & May, J. 2008, *Astrophysics*, 51, 18
- Huchtmeier, W. 1974, *A&A*, 32, 335
- Inoue, T., & Fukui, Y. 2013, *ApJ*, 774, L31
- Kaneda, H., Nakagawa, T., Ghosh, S. K., et al. 2013, *A&A*, 556, A92
- Kudryavtseva, N., Brandner, W., Gennaro, M., et al. 2012, *ApJ*, 750, L44
- Lada, C. J., & Lada, E. A. 2003, *ARA&A*, 41, 57

- Ladd, N., Purcell, C., Wong, T., & Robertson, S. 2005, *PASA*, 22, 62
- Leung, C. M., Herbst, E., & Huebner, W. F. 1984, *ApJS*, 56, 231
- McGee, R. X., & Newton, L. M. 1981, *MNRAS*, 196, 889
- Ohama, A., Dawson, J. R., Furukawa, N., et al. 2010, *ApJ*, 709, 975
- Portegies Zwart, S. F., McMillan, S. L. W., & Gieles, M. 2010, *ARA&A*, 48, 431
- Rodgers, A. W., Campbell, C. T., & Whiteoak, J. B. 1960, *MNRAS*, 121, 103
- Smith, C. H., Bourke, T. L., Wright, C. M., et al. 1999, *MNRAS*, 303, 367
- Strong, A. W., Bloemen, J. B. G. M., Dame, T. M., et al. 1988, *A&A*, 207, 1
- Takahira, K., Tasker, E. J., & Habe, A. 2014, *ApJ*, 792, 63
- Tan, J. C., Beltrán, M. T., Caselli, P., et al. 2014, *Protostars and Planets VI*, 149
- Tasker, E. J., & Tan, J. C. 2009, *ApJ*, 700, 358
- Torii, K., Enokiya, R., Sano, H., et al. 2011, *ApJ*, 738, 46
- Torii, K., Hasegawa, K., Hattori, Y., et al. 2015, accepted for publication in *ApJ*
- Vigil, M. 2004, Master’s thesis, Massachusetts Institute of Technology
- Wilson, T. L., & Rood, R. 1994, *ARA&A*, 32, 191
- Winston, E., Wolk, S. J., Bourke, T. L., et al. 2011, *ApJ*, 743, 166
- Wolk, S. J., Bourke, T. L., Smith, R. K., Spitzbart, B., & Alves, J. 2002, *ApJ*, 580, L161
- Wolk, S. J., Bourke, T. L., & Vigil, M. 2008, *The Embedded Massive Star Forming Region RCW 38*, ed. B. Reipurth, 124

Wolk, S. J., Spitzbart, B. D., Bourke, T. L., & Alves, J. 2006, *AJ*, 132, 1100

Yamaguchi, R., Saito, H., Mizuno, N., et al. 1999, *PASJ*, 51, 791

Yamaguchi, R., Mizuno, N., Mizuno, A., et al. 2001, *PASJ*, 53, 985

Zinchenko, I., Mattila, K., & Toriseva, M. 1995, *A&AS*, 111, 95

Zinnecker, H., & Yorke, H. W. 2007, *ARA&A*, 45, 481



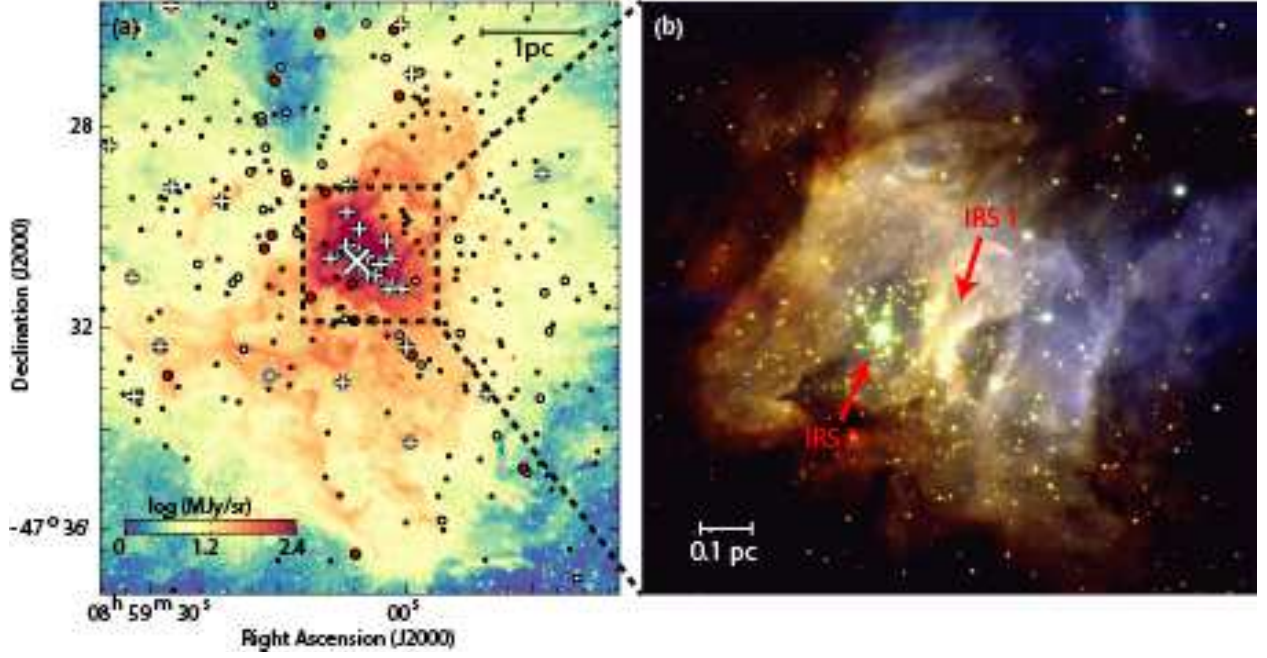


Fig. 1.— (a) The 3.6  $\mu\text{m}$  image of RCW 38 obtained with the Spitzer/IRAC observations (Wolk et al. 2008). YSOs and O star candidates obtained with Wolk et al. (2006) and Winston et al. (2011) are plotted in (b). Red circles and white circles indicate the class 0/I and flat spectrum YSOs, respectively, while black dots indicate the class II and III YSOs. White crosses indicate the candidate O stars. (b) A close-up of the central region of RCW 38 from the VLT observations (Wolk et al. 2006). Z band is shown in blue, H band is green, and K band is red. The bright infrared emission IRS 1 and IRS 2 are shown by arrows.

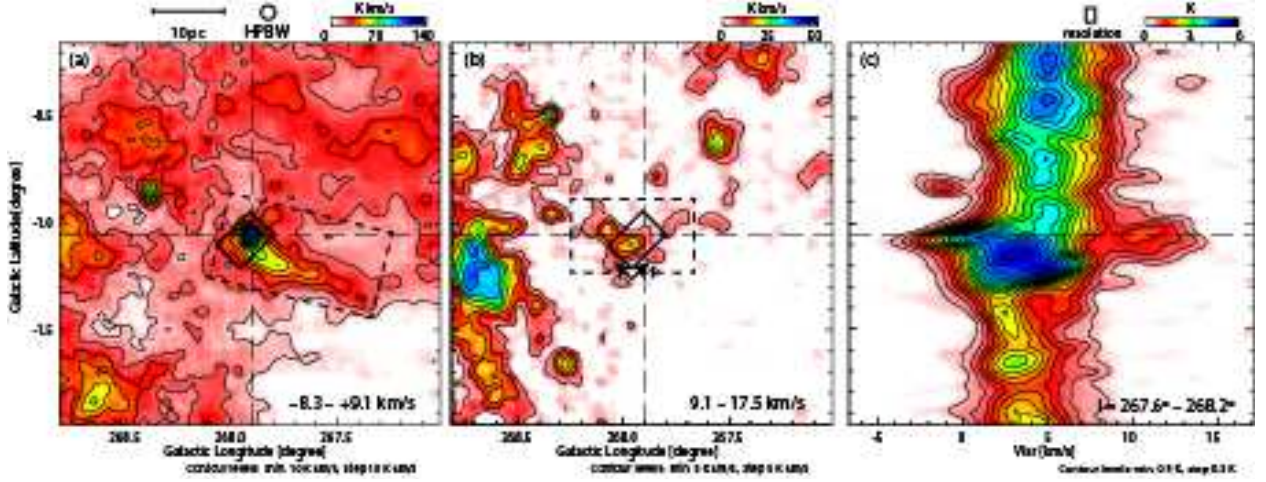


Fig. 2.—  $^{12}\text{CO } J=1-0$  integrated intensity of the red cloud (a) and the blue cloud (b). The observed area with ASTE is shown by black lines in (b). (c) Latitude-velocity diagram of the  $^{12}\text{CO } J=1-0$  emission. Dashed line indicates the position of RCW38 IRS 2.

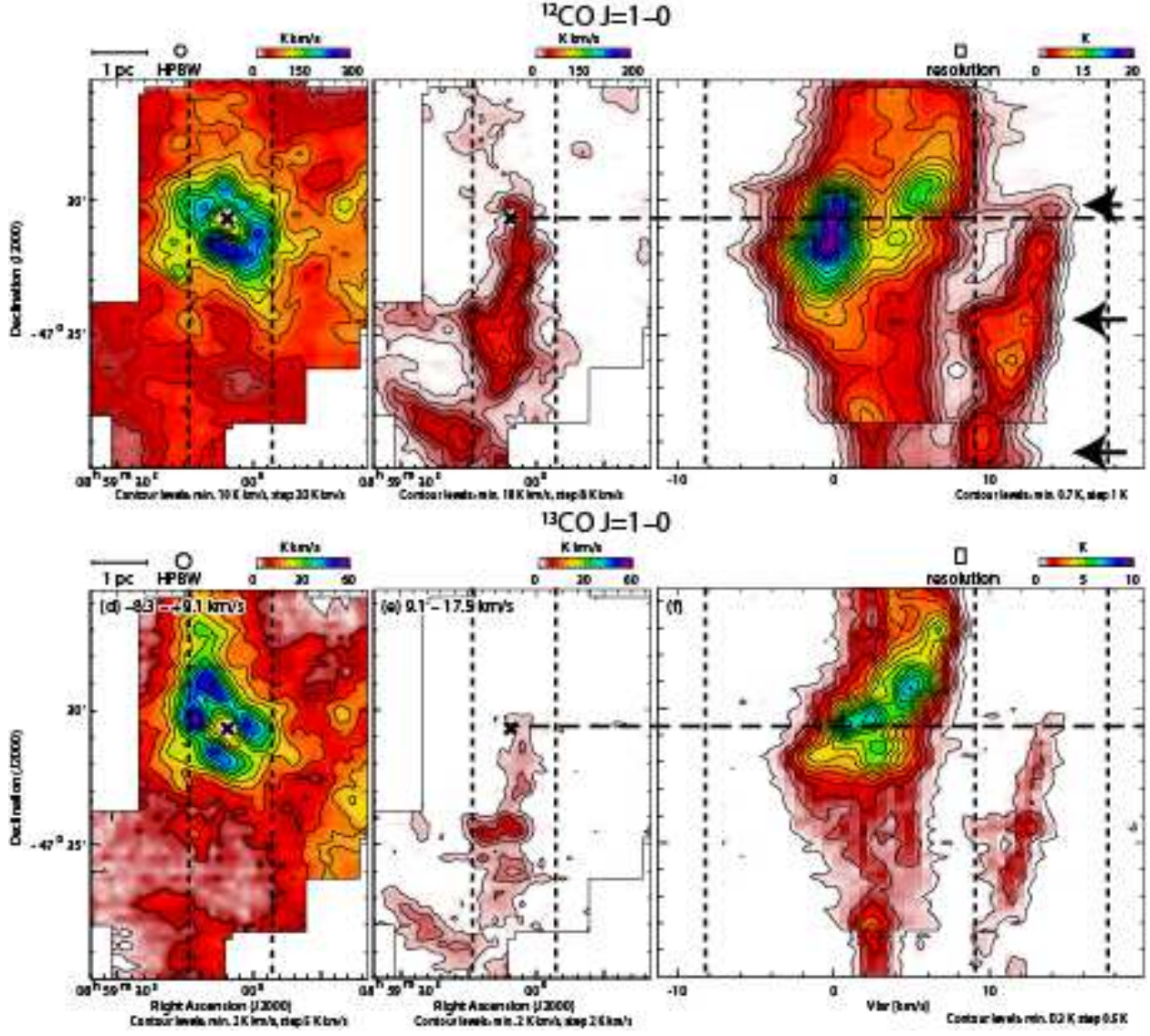


Fig. 3.— Integrated intensity maps of the blue cloud (a and d) and the red cloud (b and e) and position-velocity maps (c and f) are shown. Upper three panels show  $^{12}\text{CO } J=1-0$ , and lower three  $^{13}\text{CO } J=1-0$ .



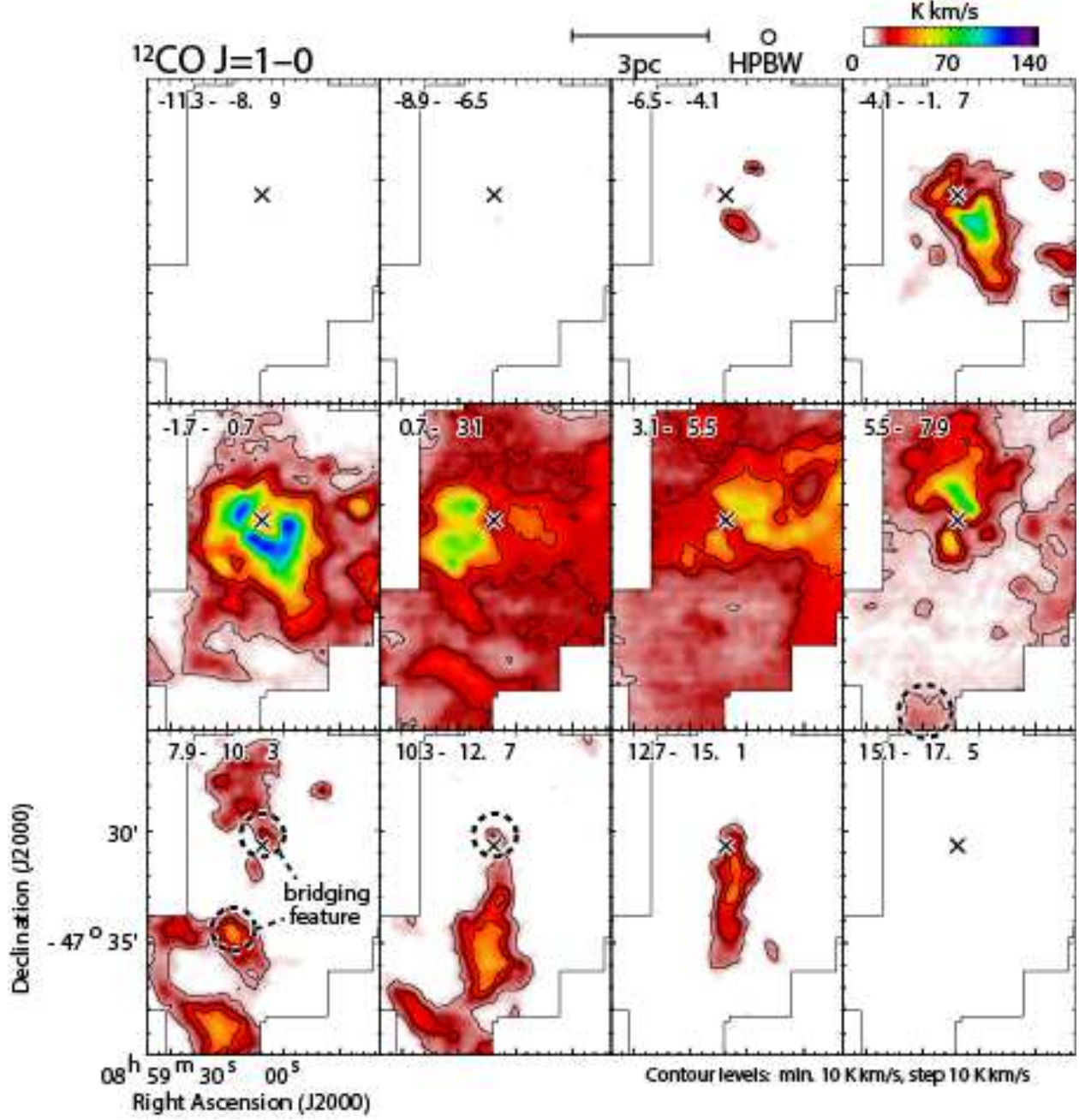


Fig. 4.— Velocity channel maps of the  $^{12}\text{CO } J=1-0$  emission obtained with Mopra. The cross in each panel indicates IRS 2.

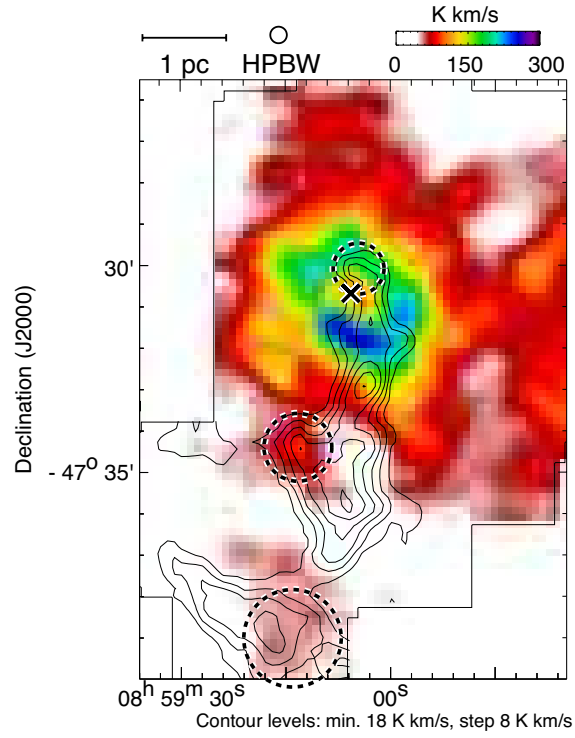


Fig. 5.— A comparison between the blue cloud (color) and the red cloud (contours) in  $^{12}\text{CO}$   $J=1-0$ .

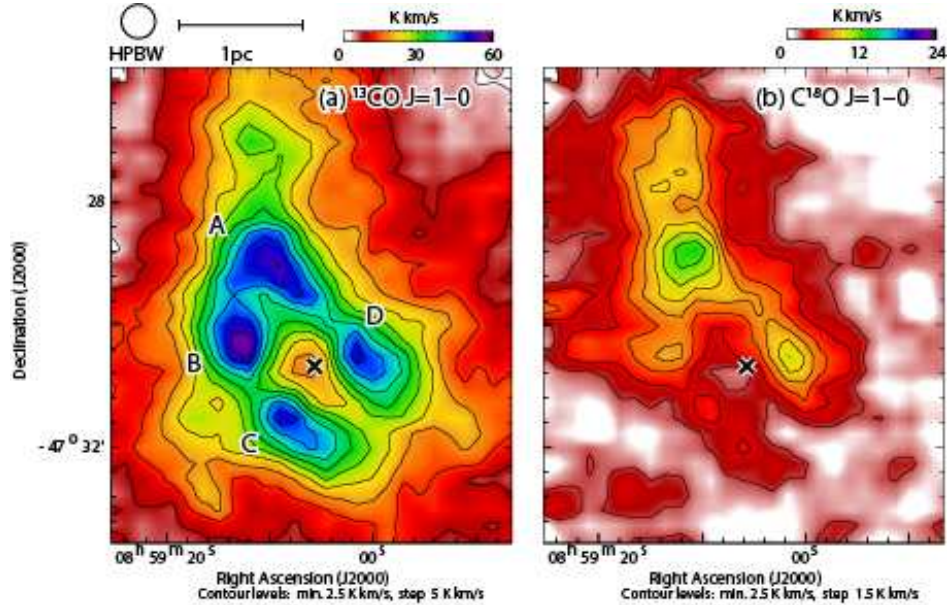


Fig. 6.— Enlarged integrated intensity maps of the blue cloud in  $^{13}\text{CO } J=1-0$  (a) and  $\text{C}^{18}\text{O } J=1-0$  for a velocity range of  $-8.3 - +9.1 \text{ km s}^{-1}$ .

Table 1: Parameters of clumps A–D

| Name    | R.A.<br>[ <sup>h</sup> <sup>m</sup> <sup>s</sup> ] | Dec.<br>[ <sup>°</sup> ' '' ] | $v_{\text{LSR}}$<br>[km s <sup>−1</sup> ] | $\Delta v$<br>[km s <sup>−1</sup> ] | size<br>[pc] | $M_{\text{LTE}}$<br>[M <sub>⊙</sub> ] |
|---------|--|-------------------------------|---|-------------------------------------|--------------|---------------------------------------|
| (1)     | (2)  | (3)                           | (4)                                       | (5)                                 | (6)          | (7)                                   |
| clump A | 8:59:9.2   | −47:29:1.5                    | 5.0                                       | 4.2                                 | 0.5          | $1.0 \times 10^3$                     |
| clump B | 8:59:12.5  | −47:30:16.9                   | 1.7                                       | 4.1                                 | 0.4          | $8.8 \times 10^2$                     |
| clump C | 8:59:8.4   | −47:31:29.7                   | 2.3                                       | 5.3                                 | 0.3          | $5.7 \times 10^2$                     |
| clump D | 8:59:1.2   | −47:30:27.3                   | 2.3                                       | 4.8                                 | 0.4          | $5.6 \times 10^2$                     |

---

Note. — Column (1): Name. (2, 3): Position in J2000. (4, 5): Peak  $v_{\text{LSR}}$  and velocity width  $\Delta v$  (FWHM) of the <sup>13</sup>CO  $J=1-0$  profile, where fitting with a Gaussian function is used to derive the parameters. (6): Size of the <sup>13</sup>CO clump.

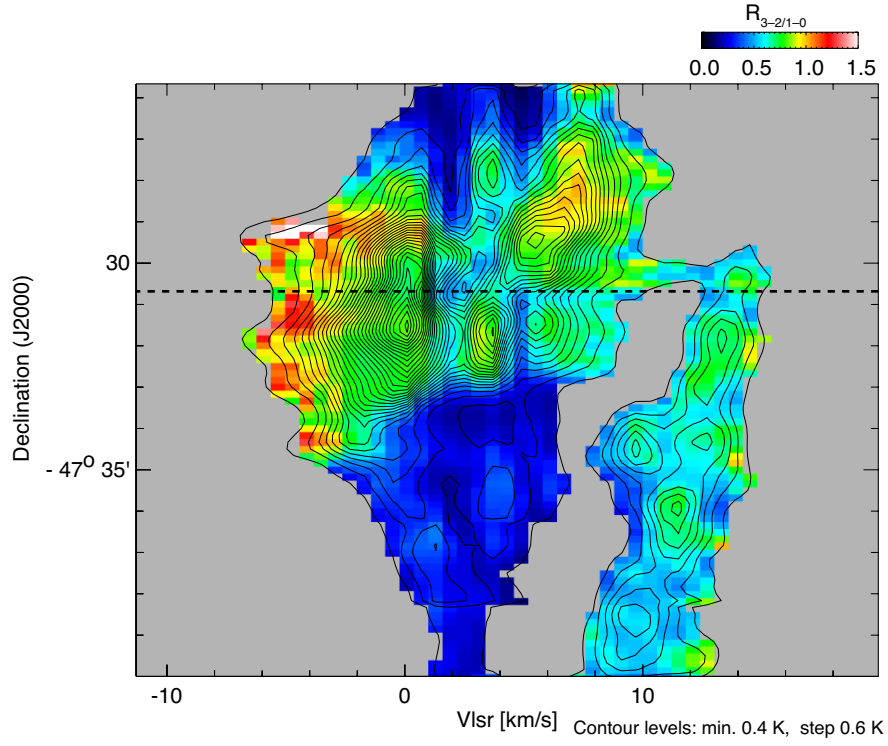


Fig. 7.— The position-velocity map of the  $^{12}\text{CO}$   $J=3-2/J=1-0$  ratio. The integration range in the R.A. is the same as Figure 3(c). The dashed line indicates the position of IRS 2.



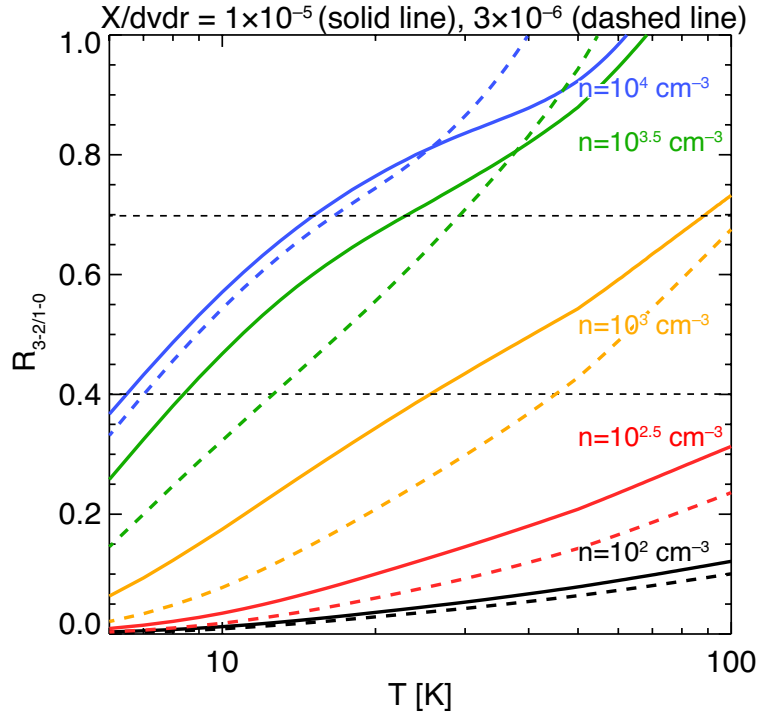


Fig. 8.— Curves of the  $^{12}\text{CO } J=3-2/J=1-0$  ratio as a function of  $T_k$  for various  $n(\text{H}_2)$  ranges estimated with LVG. Here the solid lines and dashed lines indicate  $X(\text{CO})/(dv/dr)$  of  $10^{-5} (\text{km s}^{-1} \text{ pc}^{-1})^{-1}$  and  $3 \times 10^{-6} (\text{km s}^{-1} \text{ pc}^{-1})^{-1}$ , respectively.

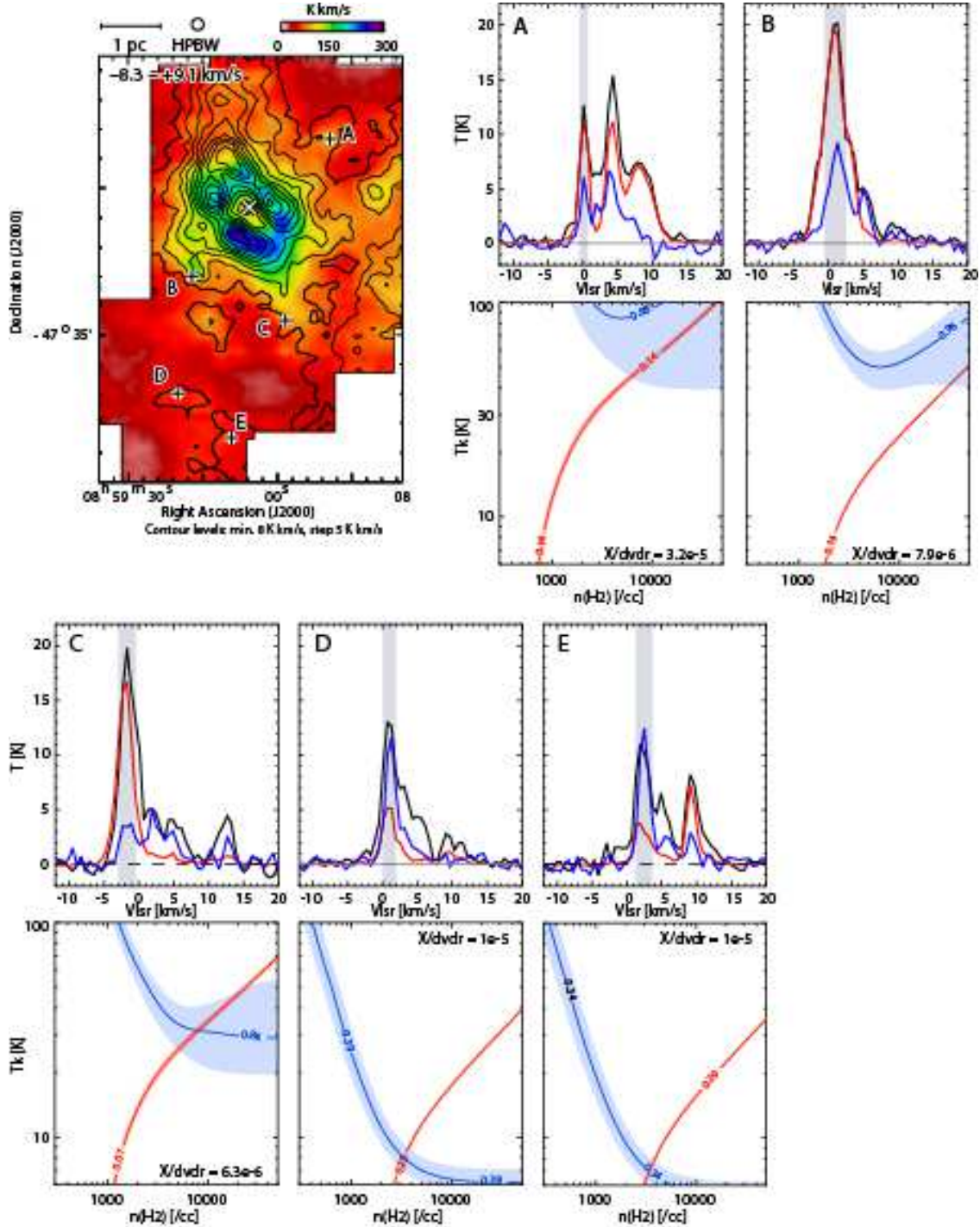


Fig. 9.— LVG results on the  $n(\text{H}_2)$ - $T_k$  plane for the regions A–E in the blue cloud are shown.  $^{12}\text{CO } J=3-2/J=1-0$  is plotted in black, and  $^{13}\text{CO}/^{12}\text{CO } J=1-0$  is in red. The regions A–E are plotted with black crosses in the CO integrated intensity map, where  $^{12}\text{CO } J=3-2$  is shown in color, while  $^{13}\text{CO } J=1-0$  is shown with contours. Spectra of  $^{12}\text{CO } J=1-0$  (black),  $^{12}\text{CO } J=3-2$  (black), and  $^{12}\text{CO } J=1-0$  (blue) are also shown. Intensities of the  $^{13}\text{CO } J=1-0$  spectra are multiplied by three.

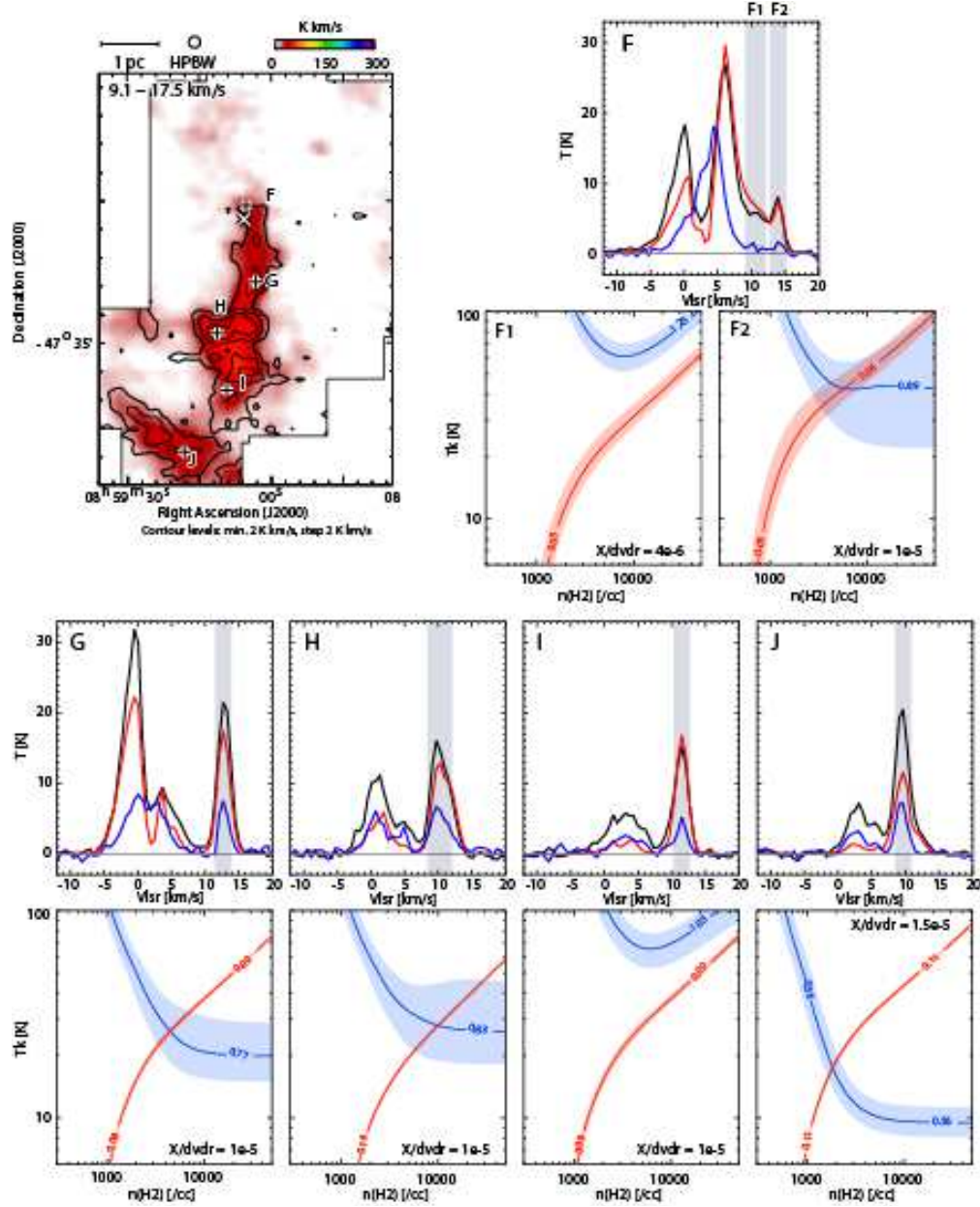


Fig. 10.— LVG results for the regions F–J in the red cloud in the same manner as Figure 14.

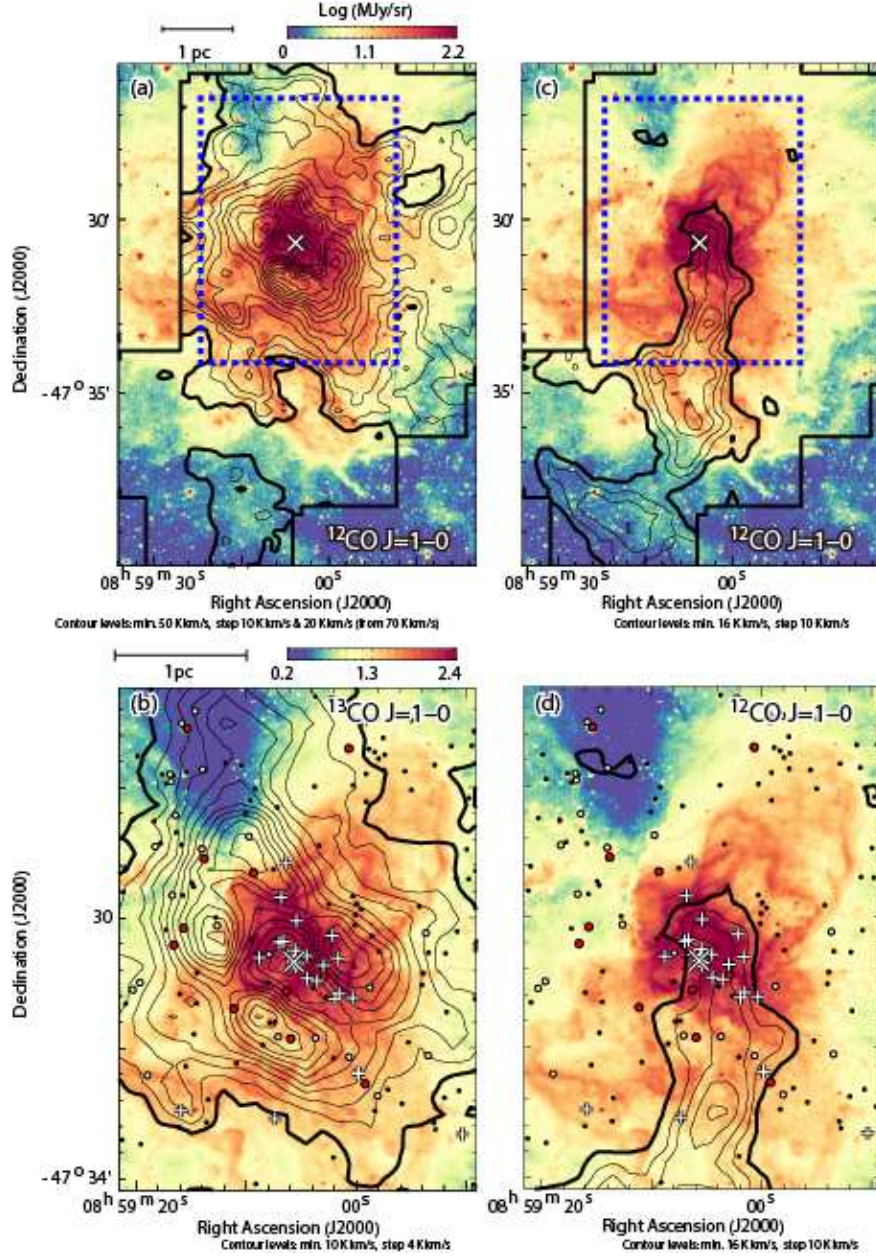


Fig. 11.— Comparisons between the two molecular clouds (contours) and the Spitzer 3.6  $\mu\text{m}$  image. The velocity ranges for (a) and (b) and for (c) are  $-8.5$ – $+9.1$   $\text{km s}^{-1}$  and  $+9.1$ – $+17.5$   $\text{km s}^{-1}$ . YSOs and O star candidates are plotted with the same manner as in Figure ??.



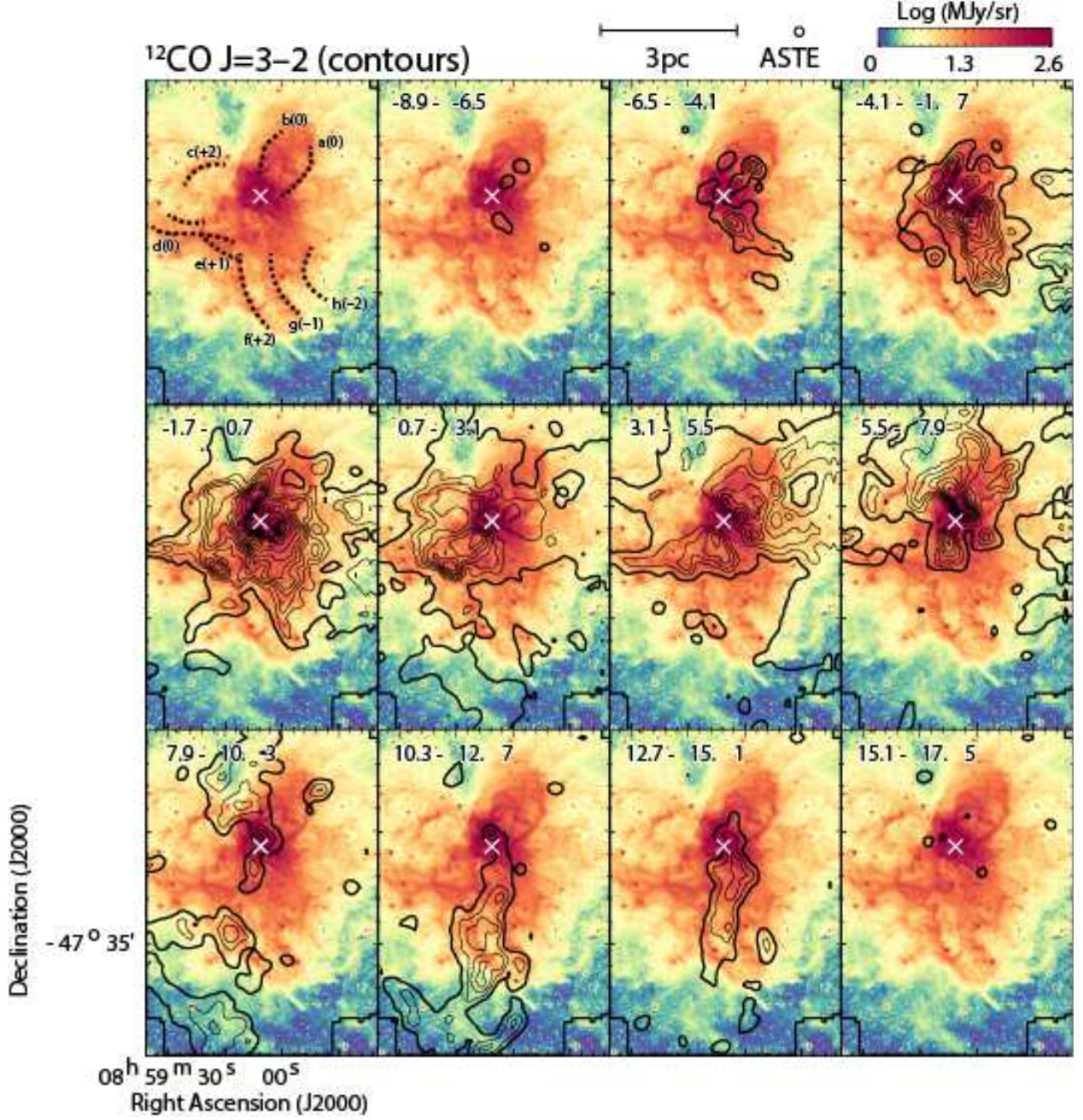


Fig. 12.— Velocity channel maps of the  $^{12}\text{CO } J=3-2$  emission (contours) superimposed on the Spitzer  $3.6\ \mu\text{m}$  image. In the left-top panel, approximate distributions of the infrared filaments (filaments a–h) are depicted by the dashed lines. The parenthetic numbers indicate peak velocities of the filaments in  $\text{km s}^{-1}$ .

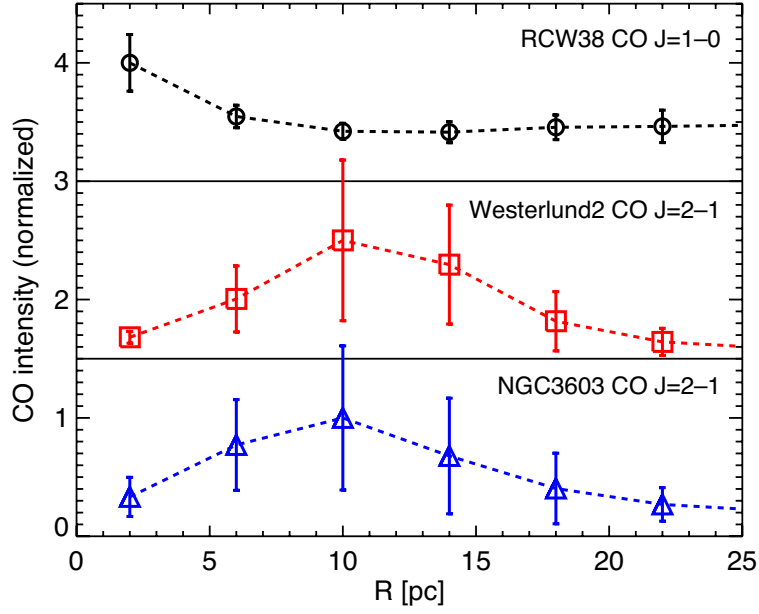


Fig. 13.— Radial distributions of the three SSCs; RCW 38 (top), Westerlund 2 (middle), and NGC 3603 (bottom). In RCW 38 the NANTEN2 CO  $J=1-0$  data set is used, while in the other two NANTEN2 CO  $J=2-1$  data sets presented in Furukawa et al. (2009) and Fukui et al. (2014) are used.